Research Paper

A Novel Multimodal NIR-II Nanoprobe for the Detection of Metastatic Lymph Nodes and Targeting Chemo-Photothermal Therapy in Oral Squamous Cell Carcinoma

Yufeng Wang[1,2*], Wansu Zhang[3*], Pengfei Sun[3], Yu Cai[2], Wenguang Xu[1,2], Quli Fan[3✉], Qingang Hu[1,2✉], Wei Han [1,2✉]

1. Department of Oral and Maxillofacial Surgery, Nanjing Stomatological Hospital, Medical School of Nanjing University, No 30 Zhongyang Road, Nanjing 210008, China.
2. Central Laboratory of Stomatology, Nanjing Stomatological Hospital, Medical School of Nanjing University, No 22 Hankou Road, Nanjing 210093, China.
3. Key Laboratory for Organic Electronics and Information Displays & Jiangsu Key Laboratory for Biosensors, Institute of Advanced Materials (IAM), Jiangsu National Synergetic Innovation Center for Advanced Materials (SICAM), Nanjing University of Posts & Telecommunications, No 9 Wenyuan Road, Nanjing 210023, China.

*These authors contributed equally to this work.

✉ Corresponding authors: Wei Han, Department of Oral and Maxillofacial Surgery, Nanjing Stomatological Hospital, Medical School of Nanjing University, Nanjing, China. Phone: +86-025-83620140; Fax: +86-025-83620140; E-mail: doctorhanwei@hotmail.com; Qingang Hu, Department of Oral and Maxillofacial Surgery, Nanjing Stomatological Hospital, Medical School of Nanjing University, Nanjing, China. Phone: +86-025-83620202; Fax: +86-025-83620202; E-mail: qghu@nju.edu.cn; Quli Fan, Key Laboratory for Organic Electronics and Information Displays & Jiangsu Key Laboratory for Biosensors, Institute of Advanced Materials (IAM), Jiangsu National Synergetic Innovation Center for Advanced Materials (SICAM), Nanjing University of Posts & Telecommunications, Nanjing, China. Phone: +86-025-83620173; Fax: +86-025-83620173; E-mail: iamqlfan@njupt.edu.cn.

Abstract

Current surgical treatment for oral squamous cell carcinoma (OSCC) must be as precise as possible to fully resect tumors and preserve functional tissues. Thus, it is urgent to develop efficient fluorescent probes to clearly identify tumor delineation, as well as metastatic lymph nodes. Chemo-photothermal therapy combination attracted a growing attention to increase anti-tumor effect in various types of cancer, including OSCC. In the present study, we designed a multimodal NIR-II probe that involves combining photothermal therapy with chemotherapy, imaging OSCC tumors and detecting metastatic lymph nodes.

Methods: In this study, we synthesized a novel near infrared (NIR)-II probe named TQTPA [4,4'-((6,7-bis(4-(hexyloxy)phenyl)-[1,2,5]thiadiazolo[3,4-g]quinoxaline-4,9-diyl)bis(thiophene-5,2-diyl))bis(N,N-diphenylaniline)] via the Suzuki reaction and prepared multimodal nanoparticles (NPs) loading TQTPA and *cis*-dichlorodiammine platinum (CDDP) (HT@CDDP) by hyaluronic acid. The characteristics of the NPs, including their photothermal and imaging capabilities were investigated *in vitro* and *in vivo*. Their anti-tumor efficacy was evaluated using orthotopic, tongue tumor-bearing, nude mice.

Results: The NPs possessed good stability and water solubility and were pH/hyaluronidase sensitive. The good tissue penetration quality and active targeting ability enabled the NPs to draw the outline of orthotopic tongue tumors and metastatic lymph nodes as small as 1 mm in nude mice by IR-808 under NIR exposure. *In vitro* and *in vivo* experiments validated the biocompatibility and low systematic toxicity of the NPs. At the same time, the NPs acted as multimodal therapy agents, combining photothermal therapy with chemotherapy.

Conclusion: With a good imaging capability and anti-tumor efficacy, our NPs successfully outlined orthotopic tongue tumors and metastatic lymph nodes as well as enabled chemo-photothermal therapy combination. Our study established a solid foundation for the application of new clinical diagnosis and treatment patterns in the future.

Key words: NIR-II imaging, chemo-photothermal therapy, active targeting, metastatic lymph node detection

Introduction

Over the past decades, limited improvements have been made in the 5-year survival rate of oral squamous cell carcinoma (OSCC) patients in spite of the availability of a multidisciplinary modality treatment [1, 2]. The leading causes for treatment failure might be related to incomplete resection of tumor tissues and neglected metastatic lymph nodes, especially the tiny ones, which in turn causes a postoperative recurrence and locoregional metastasis [3]. Surgery is the most effective treatment in OSCC, but surgery trauma inevitably affects the functions and aesthetics of the orofacial region [4]. Hence, surgical treatments must be precise and, upon complete removal of cancerous tissue, surgery should preserve normal tissue and organs as much as possible. Another feature of OSCC is the complicated lymph node drainage. Identifying metastatic lymph nodes intraoperatively is essential in determining the scope of lymph node dissection. Furthermore, some tiny metastatic lymph nodes are often neglected during traditional neck dissection [5]. At present, physicians obtain information about tumor location, size, and metastatic lymph nodes mostly by palpation and computed tomography (CT) examination, which can miss the detection of residual tumor tissues and metastatic lymph nodes [6]. Thus, clearly drawing the outline of OSCC tumor and establishing a new method to identify metastatic lymph nodes intraoperatively is extremely important to the survival rate of OSCC patients [7]. Currently, research interests in near-infrared (NIR), fluorescence-based imaging have become popular as NIR can be utilized to observe biological processes non-invasively in living subjects with high sensitivity and biological safety and without the use of ionizing radiation [8-16]. Many materials have been used in NIR imaging and cancer therapy in recent years, including antimonene, quantum dots and borophene [17-23]. Zhang et al. used black phosphorus as a biodegradable drug delivery system, realizing NIR imaging of tumors and smart NIR-light-controlled drug release for cancer therapy, which showed an excellent anti-tumor effect [24-25]. Most studies, however, have focused on first-window materials, with wavelengths ranging from 650 to 950 nm (NIR-I), such as the most widely-applied, FDA-approved small molecule indocyanine green (ICG) [26]. ICG has been used in many clinical applications, such as tumor imaging and the detection of draining lymph nodes [27]. However, ICG has shortcomings as a NIR-I probe due to photon scattering in biological tissues and the non-ignorable background signal of normal tissue, which leads to poor image resolution and clinical limitations [28]. Consequently, imaging in the NIR-II region (1000 to 1700 nm) has attracted much attention. Compared with NIR-I probes, NIR-II probes have less interference by endogenous substances in living organisms, thereby enabling deeper penetration depths and lower tissue background signals [29-36]. Previous studies have used NIR-II probes to image and observe tumors, vascular systems, and lymph node drainage. Hong et al. reported a probe, Ga-CHS$_2$, for tumor delineation and NIR-II imaging guided surgery to dissect xenograft tumors, but they did not combine image-guided surgery with other therapies [37]. Cheng et al. synthesized a novel NIR-II molecule, CQS1000, for many uses, such as the evaluation of circulatory system, assessment of tumor angiogenesis and imaging of lymphatic drainage [8]. Although there are a lot of studies on NIR-II materials at present, few reports combining the characteristics of materials with cancer therapy in the field of OSCC. Previous studies focused on the NIR-II imaging capabilities, but did not investigate its multimodal potential. Therefore, it is essential to explore a variety of capabilities of NIR-II molecules, such as photothermal therapy (PTT). Moreover, the xenograft models used in most studies hardly mimicked the true condition of the tumor. Therefore, we have established an OSCC orthotopic model using OSCC cell lines in nude mice for our *in vivo* study, rather than the common subaxillary tumor models, to simulate the growth of OSCC in living subjects [38, 39].

In addition to surgery, chemotherapy is widely regarded as one of the major treatments for OSCC [3]. CDDP [*cis*-dichlorodiammine platinum] is one of the first-line chemotherapeutic drugs for OSCC patients. However, as a solid tumor, OSCC exhibits a hypoxic microenvironment which leads to chemoresistance, especially the so-called cancer stem cells (CSCs) [40-45]. Therefore, to account for this deficiency, other therapies are often combined with chemotherapy. PTT is considered to be a novel and effective method to destroy tumor cells, converting light energy into heat energy [46-47]. Currently, researchers are focused on increasing chemo- and photothermal therapeutic effect while simultaneously decreasing side effects. Nano drug delivery systems have received much attention in recent years. Through the enhanced permeability and retention (EPR) effect, nanoparticles (NPs) can accumulate in tumor sites, reducing side effects to normal tissues [48-50]. Compared with conventional NPs, tumor-targeted NPs can enter cells through receptor-mediated endocytosis on the surface of cancer cells, thereby increasing the concentration of NPs in tumor tissues. Hyaluronic acid (HA) is an ideal, biocompatible nano-carrier and it is one of the main components of the extracellular matrix [51]. In addition, HA is one of

the ligands of CD44, which is highly expressed at the OSCC cellular membranes [52]. As one of the markers of CSCs, CD44 participates in a variety of cell signal transduction pathways and is closely related to tumor growth, proliferation, and metastasis [53,54]. Therefore, HA, as a nano-carrier, can achieve passive enrichment in tumors via the EPR effect and can actively target tumor cells with high CD44 expression.

This paper reports, for the first time, new tumor-targeted NPs (HT@CDDP) for NIR-II imaging and combined chemo-PTT, as schematically illustrated in **Figure 1**. We synthesized HT@CDDP NPs with the following considerations: (1) organic molecule, TQTPA [4,4'-((6,7-bis(4-(hexyloxy)phenyl)-[1,2,5]thiadiazolo [3,4-g]quinoxaline-4,9-diyl)bis(thiophene-5,2-diyl))bis(N,N-diphenylaniline)], was synthesized as the NIR-II-absorbing material and (2) HA was used to encapsulate CDDP and TQTPA, enhancing the targeting ability and accumulation of NPs in tumors. Through *in vivo* study, we demonstrated that the NPs accumulated at tumor sites, delineating the tumor and enabling sensitive imaging of metastatic lymph nodes in the NIR-II range. In addition, the NPs produced an anti-tumor effect in OSCC orthotopic models. The combination of HT@CDDP NPs with chemotherapy and PTT improved the anti-tumor effect to a great degree. Together, the *in vivo* and *in vitro* results revealed that the NPs could not only play an important role in tumor and metastatic lymph node imaging but also enable enhanced anti-tumor effects of chemotherapy and PTT. Thus, the NP-based NIR-II probe shows a great potential for a possible clinical use in the future.

Methods

Materials

Sodium HA (molecular weight 12–14 kDa) was purchased from Freda Biochem Co. Ltd. (Shandong, China). CDDP was purchased form Sigma–Aldrich (St. Louis, MO, USA). All antibodies were purchased from Abcam (Cambridge, UK). TQ and TPA were obtained from SunaTech Inc(Suzhou Industrial Park, Jiangsu, China). Dulbecco's modified Eagle's medium (DMEM, Gibco, America), phosphate buffer saline (PBS, Gibco, America) and fetal bovine serum (FBS, Gibco, America) were purchased from Gene Tech Co. (Shanghai, China).

Synthesis of TQTPA

TQTPA was synthesized via the Suzuki reaction between 4,9-bis-(5-bromo-thiophen-2-yl)-6,7-bis-(4-hexyloxy-phenyl)-2-thia-1,3,5,8- tetraaza cyclopenta[b]naphthalene (TQ) and diphenyl-[4-(4,4,5,5-tetramethyl-[1,3,2] dioxaborolan-2-yl)-phenyl]-amine (TPA). The TQTPA molecule has a donor-acceptor-donor (D-A-D) structure, in which triphenylamine acts as the electron donor, and TPA acts as the electron acceptor. The obtained TQTPA molecule was characterized by ^{1}H NMR, high resolution mass spectrometry, 13C NMR and MALDI- TOF.

Synthesis of HT@CDDP

We synthesized HT@CDDP using ultra-sonication. Briefly, we co-dissolved HA (20 mg) and CDDP (2 mg) in deionized water (10 mL) to obtain Solution A. Then, we dissolved TQTPA (2 mg) in THF [Tetrahydrofuran] (2 mL) to obtain Solution B. Solution A was sonicated via an ultrasound probe at a power of 180 W. Solution B was added dropwise at room temperature into
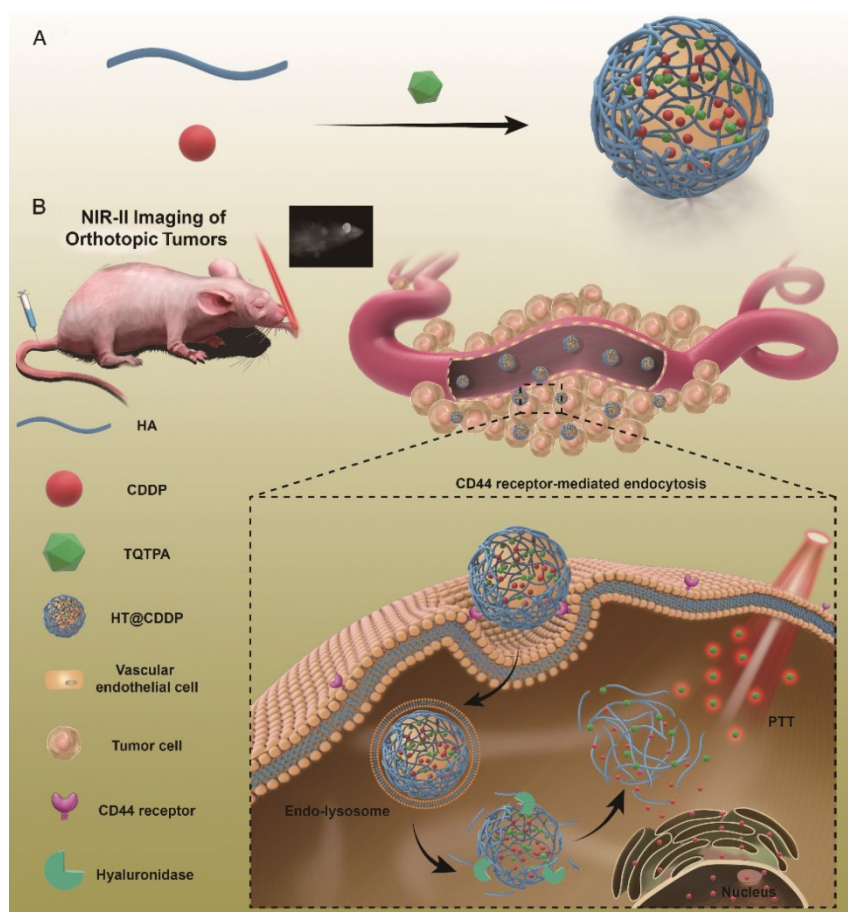

Figure 1. The schematic illustration of the preparation and application of HT@CDDP NPs. (A) A schematic illustration of the preparation of HT@CDDP NPs. **(B)** NIR-II imaging/PTT applications of HT@CDDP NPs in orthotopic OSCC tumors.

Solution A with ultra-sonication for 5 min to prepare HT@CDDP. We removed the unloaded TQTPA and free CDDP using a 30-K ultrafiltration tube at 5000 rpm for 20 min and washed them with deionized water three times. We collected the filtrate in the lower portion of the tube to measure the amount of unloaded TQTPA and free CDDP. We collected the concentrated HT@CDDP solution in the upper part of the tube for the following experiments.

Encapsulation efficiency (EE) of CDDP- and TQTPA-loaded particles

We detected the concentration of CDDP using AAS [Atomic Absorption Spectroscopy] and recorded the concentration of TQTPA using a multifunctional continuous spectrometer. We calculated the NP encapsulation efficiency (EE) as follows:

$$EE(\%) = \frac{W_0 - W_t}{W_0} \times 100\%,$$

where W_0 and W_t are the weight of the initial CDDP (TQTPA) and the total amount of CDDP (TQTPA) detected in the filtrate solution after ultrafiltration, respectively.

NP characterization

NMR spectra were recorded on a Bruker Ultra Shield Plus [Bruker BioSpin Scandinavia AB Vallgatan 5, SE-170 67 Solna, Sweden] 400 MHz spectrometer (^{1}H, 400 MHz) using tetramethylsilane (TMS) as the internal reference. We used dynamic light scattering (DLS) and transmission electron microscopy (TEM) to characterize the particle size and morphology. TEM images were performed on a HT7700 transmission electron microscope operating at an acceleration voltage of 100 kV. DLS studies were conducted using a commercial laser light scattering spectrometers (ALV-7004; ALV, Langen, Germany) equipped with a multi-τ digital time correlator and a He–Ne laser (at λ = 632.8 nm). A CONTIN analysis was used to extract the ⟨Rh⟩ data from the scattering intensity. All test samples were prepared and made optically clean by filtration through 0.45-mm Millipore filters before measurement and each sample was tested three times. The scattering angle was 90° and all measurements were carried out at room temperature. For all the samples, the final concentration of CPs was 0.1 mg mL^{-1}. We conducted spectrophotometry measurements on a Shimadzu UV-3600 UV-vis-NIR spectrophotometer [Kanda-nishiki-cho 1-chome Chiyoda-ku, Tokyo 101-8448, Japan]. The NIR-II fluorescence spectrum of TQTPA and NPs in the region of 900 - 1500 nm was measured using a NIR-II spectroscopy (Fluorolog 3) with InGaAs NIR detector under an 808-nm diode laser (RMPC lasers) excitation. To examine the ability of the NIR-II signal of the NPs to penetrate muscle, we used chicken breast tissues with different thicknesses to cover a tube filled with HT@CDDP NPs and measured the decayed NIR-II signal.

Release rate of CDDP from NPs

NPs were dissolved in 1 mL of phosphate-buffered saline (PBS) and placed in a sealed dialysis tube (MW cut-off 8000–10,000 Da, Wako, Japan). The dialysis bag was then submerged in 50-mL tubes (Falcon, BDLabware, NJ) containing 40 mL sodium phosphate buffer (50 mM) of different pH (7.4, 6.8 and 5.2), with or without hyaluronidase, and incubated in a water bath at 37 °C with reciprocal shaking at 1 Hz. The CDDP released from the dialysis bags was collected at scheduled time intervals and its amount was quantified by AAS.

Temperature increase curve *in vitro*

We used a NIR laser (808 nm, power density of 0.5, 1, and 1.5 W cm^{-2}) to irradiate the PBS solution (pH 7.4) of HT@CDDP ([TQTPA] = 0, 37.5, 75, 150, 300 μg mL^{-1}) for 5 min at an initial temperature of 25°C. We recorded the temperature values of the HT@CDDP solution at different time points using an IR thermal imager. To obtain the heating and cooling curve, the PBS solution of HT@CDDP ([TQTPA] = 300 μg mL^{-1}) was irradiated with a NIR laser (808 nm, 1.5 W cm^{-2}). Irradiation was ceased when a maximum temperature was reached, and the solution was subsequently cooled to room temperature. We repeated this process three times.

NIR-II fluorescence imaging setup

The NIR-II fluorescence imaging system was designed and built for *in vivo* and *in vitro* fluorescence imaging in the second near-infrared fluorescence range (1000−1700 nm), with a 640-by -512 pixel, two-dimensional InGaAs array (Princeton Instruments). The excitation source was an 808-nm diode laser at a power density of 40 mW cm^{-2}, and the emission light was collected through various long pass filters (980 nm) as required and focused onto the detector by a 50-mm lens.

In order to determine the detection depth of HT@CDDP NPs, we placed the HT@CDDP NPs in a tube covered by chicken breast tissues with different thicknesses (1 mm, 3 mm, 6.5 mm, 9 mm, 12 mm, and 15mm), as shown in the Supplementary Material.

Cell culture

Human oral squamous cell carcinoma lines, HSC3 and SCC4, were kindly provided by the Ninth Hospital of Shanghai. They were cultured in DMEM with 10% FBS, 100 U mL^{-1} penicillin and 100 mg mL^{-1} streptomycin at 37 °C in a humidified atmosphere

containing 5% CO2 and 95% air.

Cellular uptake efficiency

We seeded HSC3 and SCC4 cells in 6-well plates at a density of 5.0×10^4 cells and cultured them for 24 h, followed by a treatment with HT@CDDP NPs ([TQTPA] = 0.1 mg mL^{-1}) in a normal culture medium and in a culture medium with anti-CD44 antibody, respectively. After incubating for 1 h, 9 h, 13 h, and 20 h, the cells were digested with trypsin (EDTA) and centrifuged at 1000 rpm for 5 min. The cells were then washed three times with PBS to remove the remaining culture medium, and they were reseeded in 96-well plates in PBS (100 µL). The 96-well plates were irradiated with the NIR-II fluorescence imaging system to measure the NIR-II signal and analyze the targeting efficiency of HT@CDDP NPs to CD44-expressing cells.

Cytotoxicity assay

The toxicities of T@CDDP [referring to free CDDP] and HT@CDDP NPs, with or without irradiation, were tested using CCK-8 [Cell Counting Kit-8]. Cells were plated in 96-well plates at densities of 5,500–6,500 cells in a 100 µL complete culture medium. Blank control wells containing the same volume of complete culture medium were included in each assay. The microplate was incubated at 37 °C until cells adhered to the plates. The cells were then washed with PBS and incubated with T@CDDP and HT@CDDP, which were serially diluted in a complete culture medium before use. The plate was further incubated for 24–36 hours. For the HT@CDDP with irradiation group, cells were exposed under an 808-nm laser at 1.0 W cm^{-2} for 10 min. CCK-8 (10 µL) was added to each well. The optical density (OD) of formazan at 450 nm was recorded every 30 minutes until the OD was 1.0–2.0. Six wells corresponded to each concentration of the aforementioned drugs. Cell viability was calculated as follows: cell viability = ([OD]$_{test}$ - [OD]$_{control}$)/([OD]$_{control}$ - [OD]$_{blank}$) ×100%.

In vivo NIR-II and ICG imaging

We administered HT@CDDP NPs in PBS solution ([TQTPA] = 1mg mL^{-1}) and ICG in PBS solution ([ICG] = 1mg mL^{-1}) to mice bearing orthotopic tongue squamous carcinoma via tail injection at a volume of 100 µL per mouse. At 0, 4, 10, 20, 24, and 30 h postinjection, mice were anesthetized and imaged via the *in vivo* NIR-II imaging system. Typically, at 30 h postinjection, we carefully removed major organs of mice, including heart, liver, spleen, lung, kidney, tumor, and lymph nodes, and rinsed the organs for visualization. We analyzed the NIR-II signal intensity using the *in vivo* NIR-II imaging system's software.

OSCC model establishment

To establish an orthotopic xenograft model of human OSCC, the human OSCC cells HSC3 (1×10^6 cells in 50 µL PBS) were submucosally inoculated into the tongues of nude mice (4 mice per group). We measured the tumor dimensions every other day by a caliper and calculated the volume by the formula (V = (L×W^2)/2, where L is tumor length and W is tumor width). When the tumor volume was approximately 12 mm^3, the mice were ready for *in vivo* anti-tumor efficacy experiments.

In vivo chemo-photothermal therapy combination

We randomly divided the tumor-bearing mice into 8 groups (n = 4). Then, the mice were administered the following: (1) saline, (2) saline with irradiation, (3) HT, (4) HT with irradiation, (5) HT@CDDP, (6) HT@CDDP with irradiation, (7) T@CDDP, and (8) T@CDDP with irradiation. The different formulations were administrated via tail vein injection (CDDP dose: 5 mg kg^{-1}). Mice of groups (2), (4), (6), and (8) received irradiation via an 808-nm laser (1.0 W) for 10 min in the tumor regions. We used a thermal imager to detect the change in temperature in tumor regions. We measured tumor volume and mice weight every other day. When the treatment was complete, we removed tissues for HE (hematoxylin and eosin) staining and immunostaining.

Statistical analysis

All data shown are expressed as the mean ± SE for at least three separate experiments unless otherwise stated. Statistical analyses were carried out using a two-tailed Student's t-test and homogeneity of variance tests (p values < 0.05 were considered significant).

Ethical statement

Institutional review board approval was obtained from Nanjing Stomatological Hospital Ethics Committee (approval number, 2017NL-003). All animal experiments and experimental protocols were in accordance with the Animal Care and Use Committee of the Medical School of Nanjing University.

Results and discussion

The synthesis and structure of TQTPA was shown as **Figure 2 and Figure S1-S4.** The fluorescence quantum yield of TQTPA in THF solution under an excitation of 808 nm was about 3.03%, measured against a standard IR1061 dye in dichloromethane as a reference. As shown in **Figure S5A**, TQTPA has

strong absorption in the NIR region, with a main absorption peak at 760 nm in THF and its extinction coefficient is 6.762 mL g^{-1} cm^{-1}. The fluorescence emission spectrum showed a maximum NIR-II emission peak at 1016 nm, using 808 nm as the excitation wavelength (**Figure S5B**). This indicates a large Stokes shift of about 256 nm.

We conducted nanoprecipitation to prepare water-soluble, semiconducting HT@CDDP NPs using the hydrophilic polymer HA as a stabilizer to encapsulate the hydrophobic molecule TQTPA and anti-cancer drug CDDP. The diameter and morphology of HT@CDDP NPs in aqueous solution were characterized with DLS and TEM (**Figure 3A**). HT@CDDP NPs had well-dispersed sphere structures, with an average diameter of 110 nm. The NPs

exhibited good water solubility and a nano-size formulation similar to many other polymeric CDDP complex/conjugates [55]. The hydrodynamic radius of the HT@CDDP NPs in different media, including PBS, FBS, and DMEM, showed no obvious difference (**Figure S6**). In **Figure 3B**, the HT@CDDP NPs also showed good NIR absorption, with a predominant absorption peak at 760 nm. The fluorescence emission spectrum showed a maximum NIR-II emission peak at 1057 nm. In addition, the HT@CDDP NPs exhibited high photo stability, zeta potential stability and size stability (**Figure S7 and S8**). NP detection depth was evaluated by NIR-II imaging for samples covered by chicken breast tissues with varying thicknesses. The NIR-II signals of the NPs decreased slightly as the thickness of the chick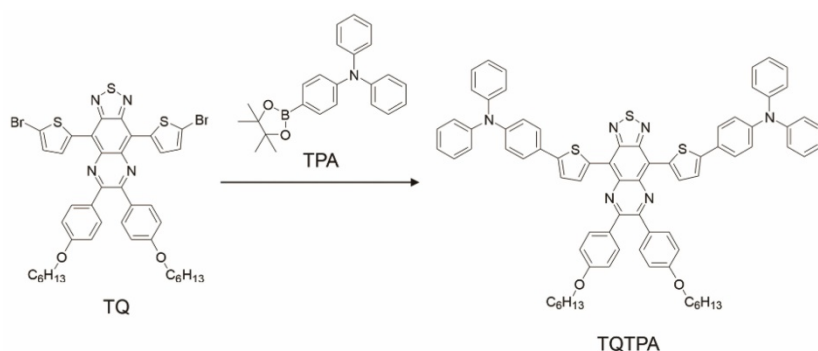en breast tissue increased from 0 to 3 mm. Notably, we found that even when the samples were covered by chicken breast tissue as thick as 6.5 mm, its NIR-II signal was still detectable (**Figure 3C-D** and **Figure S9**). Therefore, the as-prepared HT@CDDP NPs can be used in NIR-II imaging.

As reported, HA is an ideal DDS [Drug Delivery System] that can be combined with CDDP via ionic interactions between Pt^{2+} of CDDP and carboxylic acid of HA [56-59]. We used AAS to confirm the successful encapsulation of CDDP by measuring the concentration of CDDP in an HT@CDDP-containing PBS solution. In order to compare the capacity of loading CDDP between HA and PEG [polyethylene glycol], we also used PEG to load CDDP and TQTPA. The encapsulation efficiency of CDDP was 32.33%, which is higher than that when PEG is used as a nano-carrier (20.59%), which is consistent with other published studies [60, 61]. This is possibly due to the electrostatic binding between HA and CDDP.

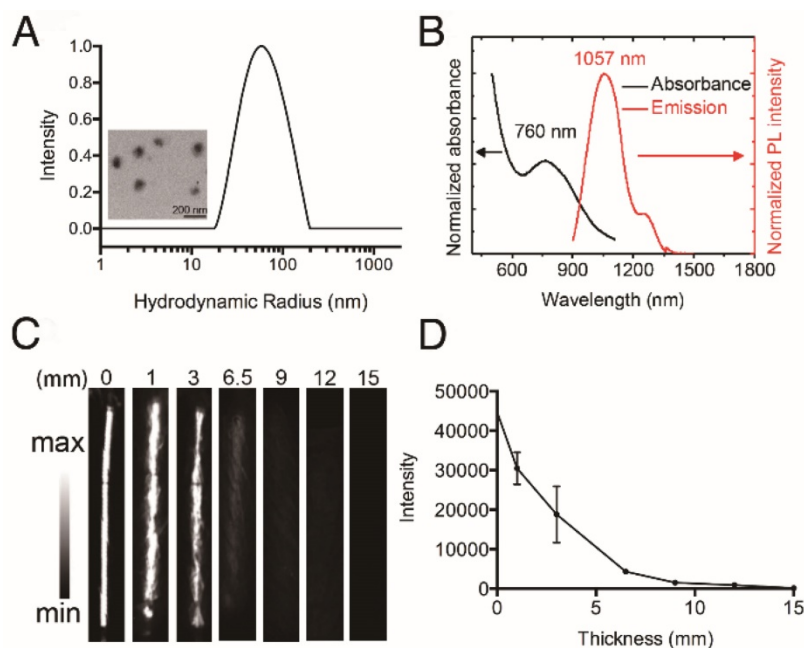**Figure 2.** Synthesis procedures for TQTPA.

Figure 3. Characterization of HT@CDDP NPs. **(A)** The hydrodynamic radius (Rh) of HT@CDDP NPs in PBS determined by dynamic light scattering (DLS) and transmission electron microscopy (TEM) image of HT@CDDP NPs. Scale bars represent 200 nm. **(B)** The absorption and fluorescence emission spectra of HT@CDDP NPs. **(C)** NIR-II imaging and **(D)** signal intensities of HT@CDDP NPs covered by chicken breast tissues with varying thicknesses. The results represent mean ± SE (n=3).

Next, we studied the *in vitro* release profile of CDDP from HT@CDDP NPs in different media. As shown in **Figure 4A**, about 12.35 ± 0.67% of CDDP was released after 16 h in PBS at pH 7.4. The release of CDDP, however, increased from 22.19 ± 0.74% to 33.84 ± 1.01% as the pH decreased from 6.8 to 5.2, respectively. This was attributed to the increase in HA dissolution in an acidic environment. These findings suggest that the weak

acidic condition of solid tumors could accelerate the release of CDDP from the HT@CDDP NPs and, upon their internalization in tumor cells via endocytosis, the lower pH of lysosomes would facilitate a more rapid release of CDDP [29]. In addition, because HA can be hydrolyzed by hyaluronidase [62, 63], we evaluated the effect of hyaluronidase on the release of CDDP from the NPs. The NPs were treated with PBS containing 150 U mL^{-1} hyaluronidase at pH 7.4 and 5.2. The addition of hyaluronidase expedited the release of CDDP to 28.34 ± 0.51% at pH 7.4 and 45.68 ± 1.26% at pH 5.2 at 16 h. This result suggests that the enriched hyaluronidase in tumor cells will facilitate the release of CDDP from NPs. Moreover, the release of NPs is influenced by pH and hyaluronidase, suggesting good stability in blood circulation and rapid release in the low pH environment of the phago-lysosomal system [56].

To study the efficiency of the HT@CDDP NPs for PTT, we exposed different concentrations of NPs to an 808-nm NIR laser (1.5 W cm^{-2}). The results in **Figure 4B** show that the temperature of the NPs increased with increasing TQTPA concentration. When TQTPA concentration reached 300 µg mL^{-1}, the solution temperature increased by 40.5 °C, which was higher than that at 0.5 W cm^{-2} (19.0 °C) and at 1.0 W cm^{-2} (27 °C) (**Figure 4C**). To evaluate the stability of the photothermal property, we performed three replications of an irradiation experiment. The heating and

cooling curve indicated that the NPs exhibited a great optical stability after three cycles of laser-induced heating (**Figure 4D**). The value of photothermal conversion efficiency was calculated out to be 22% [64, 65]. The satisfactory photothermal properties of our NPs including excellent photothermal conversion efficiency, good photo-stability and favorable absorbance features make them suitable for PTT [66].

HA is a ligand of the CD44 receptor, which is highly expressed on the cell membrane of many solid tumor cells, including OSCC. To investigate the targeting ability of the HT@CDDP NPs on OSCC cells, we selected two human OSCC cell lines with high levels of CD44 expression (**Figure S10**). We first examined the influence of blocking CD44 on the intracellular uptake of HT@CDDP NPs in OSCC cells. As shown in **Figure 5A-B**, we observed a time-dependent increase in the NIR-II signal intensity, indicating an intracellular accumulation of the HT@CDDP NPs. More importantly, the cellular uptake of the NPs was significantly suppressed by the addition of anti-CD44 antibody, emphasizing the importance of receptor-mediated endocytosis. We evaluated the cytotoxicity of the HT@CDDP NPs by a CCK8 assay. The cytotoxicity of the NPs against OSCC cells was comparable to that of T@CDDP *in vitro*. As expected, we observed an enhanced anti-tumor effect of the HT@CDDP NPs upon laser stimulation (**Figure 5C-D**). The IC$_{50}$ values of the HT@CDDP NPs with irradiation and T@CDDP were 9.863 µM and 1.281 µM in HSC3 cells, respectively (9.531 µM and 2.893 µM in SCC4 cells, respectively), confirming the excellent anti-tumor efficacy of the HT@CDDP NPs with irradiation *in vitro*.

We also conducted a flow cytometry analysis using an Annexin V-FITC/PI staining kit to evaluate the effect of the HT@CDDP NPs with or without irradiation on cell apoptosis. The results in **Figure 6** and **Figure S11-13** show the apparent enhanced cell apoptosis of HSC3 and SCC4 cells when treated with HT@CDDP NPs and stimulated with irradiation. The HT@CDDP NPs showed no obvious difference from T@CDDP on cell apoptosis at the same concentration of CDDP (IC$_{50}$). Upon irradiation, however, the number of apoptotic cells increased significantly, regardless of the presence of CDDP. This result demonstrated that HT@CDDP NPs with irradiation could promote cell apoptosis significantly *in vitro*.
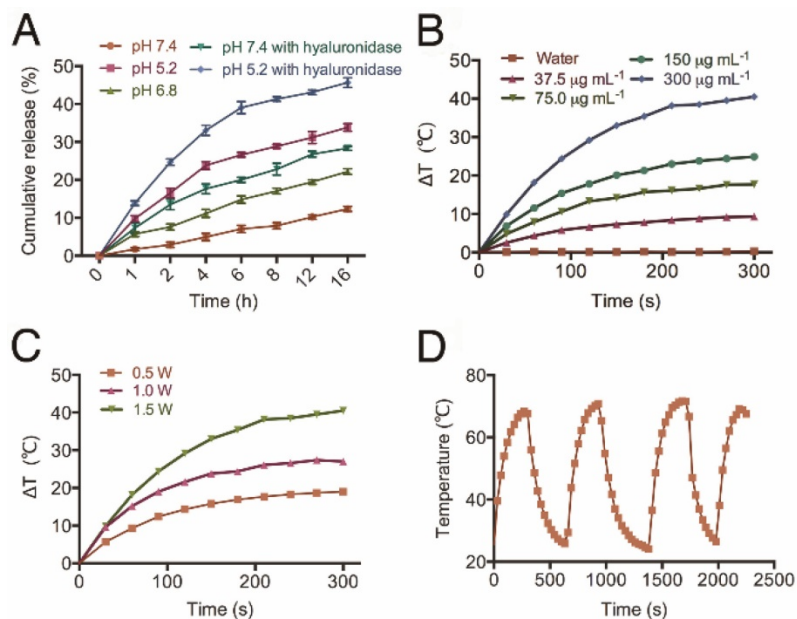

Figure 4. The release profile and photothermal property of NPs. (A) The cumulative drug release profile of HT@CDDP NPs at different pH values and in the case of hyaluronidase. The results represent mean ± SD (n=3). **(B)** The heating curves of HT@CDDP NPs at different concentrations by an 808-nm laser at a power density of 1.5 W cm^{-2}. **(C)** The heating curves of HT@CDDP NPs (300 µg mL^{-1} TQTPA) by an 808-nm laser at different radiant power values. **(D)** The heating-cooling curve of HT@CDDP NPs (300 µg mL^{-1} TQTPA) by an 808-nm laser at a power density of 1.5 W cm^{-2}.
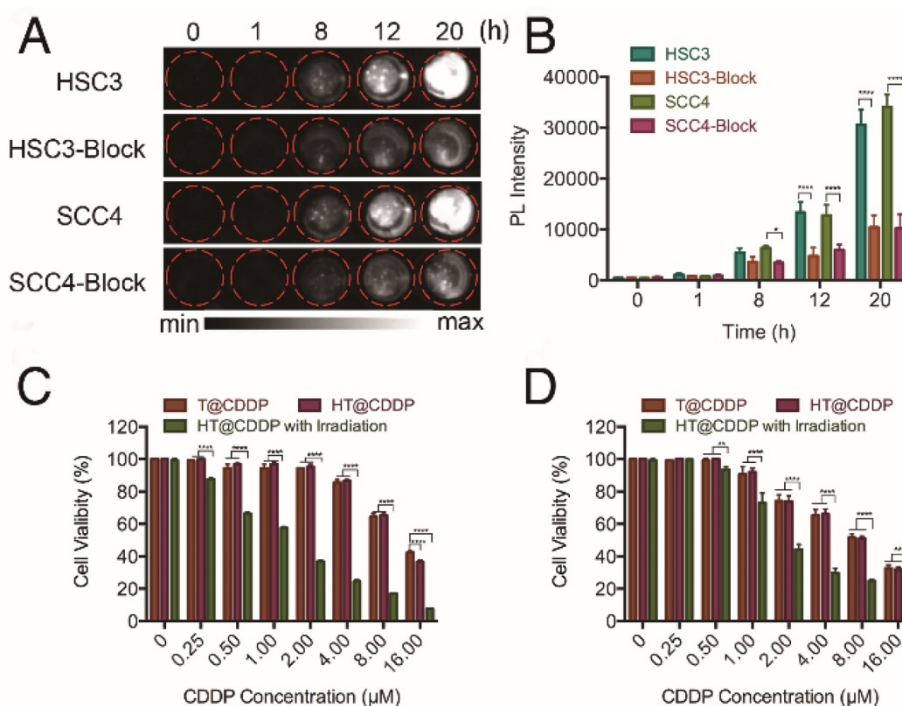
Figure 5. Cellular uptake and cytotoxity of NPs. (A) NIR-II imaging and **(B)** signal intensities of HSC3 and SCC4 cell lines with and without anti-CD44 antibody blocking after incubating with HT@CDDP NPs at different time points. **(C)** Cell viability, determined using a CCK8 assay, of T@CDDP and HT@CDDP NPs at different concentrations of CDDP with or without irradiation in HSC3 and **(D)** SCC4 cell lines. The results represent mean ± SE (n=3). *p<0.05, **p<0.01, **** p < 0.0001, ANOVA analysis.
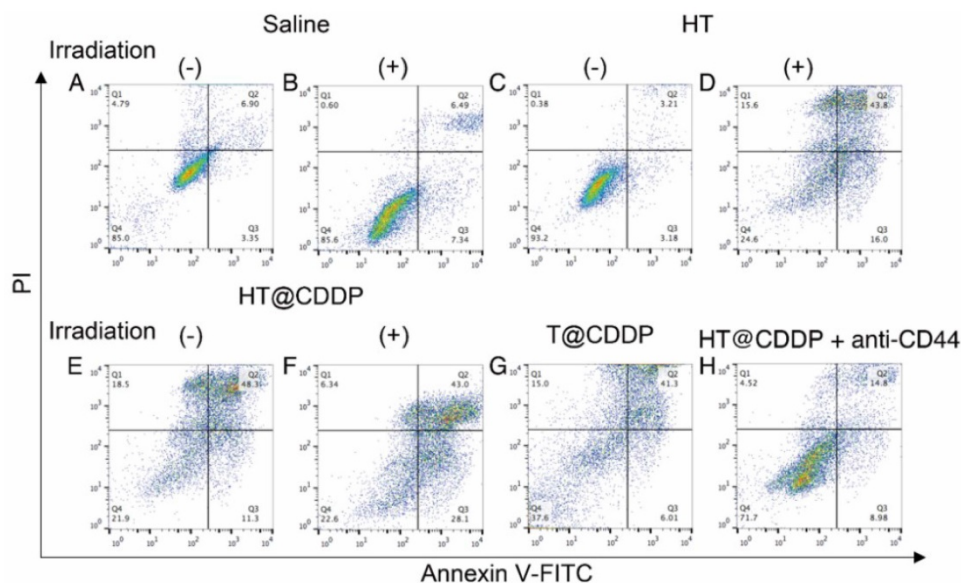

Figure 6. Cell apoptosis of HSC3 cells treated with different media and examined by Annexin V-FITC/PI staining kit and flow cytometry.

As noted, NIR-II materials possess better imaging capabilities than NIR-I materials, offering less interference by endogenous substances, lower tissue background, and higher resolution. To explore the potential of HT@CDDP as a novel NIR-II probe in living subjects, we injected the NPs into mice via their tail veins, using ICG for comparison. As shown in **Figure S14A**, at 15 min postinjection, the NIR-II images showed that the circulatory system was clearly visualized, whereas ICG gave a lower quality image with blurry features. From **Figure S14B**, the femoral artery was clearly depicted by HT@CDDP, but ICG failed to produce a distinct image of the femoral artery. The signal intensity was measured by plotting cross sections of the same vessel (femoral artery), marked by red arrows. As shown in **Figure**

S14C, an obvious peak from the HT@CDDP group was observed, with a Gaussian-fitted full width at half maximum (FWHM) of the cross-sectional intensity profile of 0.606 mm. Conversely, the intensity analysis obtained for the ICG group showed a broad, less intense peak. These findings demonstrated that the HT@CDDP NPs, as NIR imaging agents, produced better contrast and higher resolution images than the clinically-approved ICG.

After NIR imaging of HT@CDDP and ICG in blood vessels, we aimed to study the tumor imaging properties of each agent solution. Nude mice with HSC3 orthotopic xenografts were randomly divided into three groups (n = 3 per group) and arranged as: (1) ICG, (2) HT@CDDP and (3) HT@CDDP with excess HA blocking. The ICG and HT@CDDP solutions were injected in tail veils, whereas the HA PBS solution was administered through paracancerous injection 6 h ahead of the HT@CDDP injection. The mice in the ICG group were imaged with NIR-I, whereas the mice of the HT@CDDP group were imaged with NIR-II. As shown in **Figure 7**, the tumors could be clearly visualized in the NIR-II images, at different time points. The ICG-enhanced imaging, however, failed to make a distinction between the tumor nodule and the adjacent tissues, possibly due to its inherently high background signal. The enrichment of the HT@CDDP NPs in tumor regions was significantly inhibited when CD44 was blocked by HA through the HA (ligand)-CD44 (receptor) interaction. Interestingly, the tumor vascular branches could be discerned immediately after injecting ICG and HT@CDDP solutions. At 4 h postinjection, the vascular image of the ICG group disappeared, whereas the image of the HT@CDDP group was still visible. On the basis of this result, the HT@CDDP NPs show a great potential for visualizing the vascular network in tumors, observing tumor progression and assessing the efficacy of some anti-angiogenic drugs.

The signal intensity-to-background ratio (SBR) is shown in **Figure 8A** and **Figure S15**. NIR-II imaging of tumors has a high SBR, with an average value of 2.78 immediately after tail vein injection. Although the SBR declined to 2.18 at 4 h, it seemed that the HT@CDDP NPs became more homogeneously distributed at tumor region. The SBR gradually increased and reached 8.06 at 24 h, but later decreased to 3.65 at 30 h postinjection. Conversely, the SBR in the HA blocking group showed no obvious increase over 20 h, and the maximum SBR at 24 h was only about 2.35. Interestingly, a lymph node image (**Figure 7**, LN#1, green circle) with an SBR of 1.72 appeared at 10 h in the HT@CDDP group. At 20 h, the SBR of LN#1 reached 3.17, and it revealed another lymph node image (**Figure 7**, LN#2, blue circle) with an SBR

of 2.92. The SBR of LN#2 reached a maximum of 3.55 at 24 h (**Figure 8C**). On the basis of these findings, we hypothesize that the HT@CDDP NPs could be used for tumor and lymph node imaging.

To validate whether the two lymph node images represented two metastatic lymph nodes, we dissected the mice at 30 h postinjection. As shown in **Figure 8B** and **Figure S16**, the NIR-II signals were mainly enriched in tumors, livers, and spleens, suggesting a low damage to hearts and kidneys. This is an important result for assessing the *in vivo* safety of the NPs. The two excised lymph nodes were apparently displayed; LN#2 was very small, but had a strong fluorescence signal. According to HE and cytokeratin (CK) staining results in **Figure 8D**, LN#1 and LN#2 showed a positive expression of CK. Therefore, they were confirmed to be metastatic lymph nodes. However, the image of the metastatic lymph nodes appeared later than that of the tumor, but the SBRs of the tumor and the two lymph nodes achieved maximum values at about 24 h postinjection, which met the requirement of a clinical application. This provided promising evidence that the HT@CDDP NPs could accumulate at tumor sites and be used to detect metastatic lymph nodes, especially tiny ones that could be easily overlooked.

The photothermal characteristics of the HT@CDDP NPs have been confirmed *in vitro*; therefore, we further studied their potential in combined chemo-PTT. This study used an orthotopic OSCC mouse model described previously. First, we proved that the NPs exhibited excellent photothermal effects *in vivo* and used a thermal imager to monitor temperature changes. As shown in **Figure 9A-B**, the temperature of the tumor regions increased immediately upon an 808-nm (1.0 W) laser irradiation. After about 3–4 min of irradiation, the temperature reached 50.5 °C, which is sufficient to destroy tumor cells [47]. As shown in **Figure 9C-D** and **Figure S18A, C**, HT@CDDP induced a remarkable tumor growth delay and, 13 days after treatment, the tumor size $(5.70 \pm 1.14 \text{ mm}^3)$ was reduced by 82.78% compared with the untreated control $(33.11 \pm 4.63 \text{ mm}^3)$. The tumor volume of mice in the T@CDDP group, on the other hand, increased by 33.93% $(13.92 \pm 1.24 \text{ mm}^3$ at day 1 and $19.48 \pm 0.72 \text{ mm}^3$ at day 13). We then performed a histological analysis (HE, Ki67, and Bcl2 staining) to further evaluate the *in vivo* anti-tumor activity of the HT@CDDP NPs. Tumor tissues and other organs were collected on day 14. As shown in **Figure 10** and **Figure S18D**, the HT@CDDP, HT, and HT@CDDP (with laser) groups presented lower levels of the cell proliferation marker Ki67 and cell apoptosis inhibitor Bcl2 compared with the other groups. The anti-tumor effect of T@CDDP showed no obvious

difference, with or without irradiation. Therefore, both *in vivo* experiments and histological analysis are in agreement with the efficient anti-tumor effects of the HT@CDDP NPs observed *in vitro*. Thus, the HT@CDDP NPs are expected to be potential biomedicines that combine chemotherapy and PTT with effective anti-tumor abilities.

To evaluate the *in vivo* systematic toxicity of HT@CDDP, we measured the weight of mice every other day from the beginning of the treatment. As shown in **Figure S17B** and **S18B**, the weight of mice in the HT@CDDP group, with or without irradiation, did not change significantly compared with the beginning (21.50 ± 0.32 g to 20.35 ± 0.12 g with irradiation and 23.70 ± 01.14 g to 23.95 ± 0.96 g without irradiation, respectively). The slight decrease in the weight of mice in the HT@CDDP with laser group may be due to tongue pain, which was caused by heating. The mice, however, experienced an obvious decrease in weight from 24.88 ± 0.38 g to 21.02 ± 1.25 g in the control group and from 20.53 ± 1.00 g to 17.42 ± 1.33 g in the HT group. A decrease in weight was also observed in the T@CDDP group, from 22.20 ± 0.44 g to 19.48 ± 0.63 g, though without a statistical significance. H&E staining of mice hearts, livers, and kidneys also revealed that the NPs did less damage to these organs than T@CDDP (**Figure S17A** and **S18D**). To further assess the biosafety of HT@CDDP, we injected HT@CDDP PBS solution and T@CDDP into tumor-bearing mice and healthy rats via tail veins. We dissected tumors, hearts, livers and kidneys from the mice and measured CDDP content in the different organs at 7 days postinjection. In addition, we collected blood from rat orbits and used it for a serological examination to evaluate liver and renal functions at 2 and 4 weeks postinjection. The concentration of CDDP in the tumor of the HT@CDDP group was more than twofold that of the T@CDDP group. This confirmed the enrichment effect in tumor regions (**Figure S17C**). In livers, the concentration of CDDP for the HT@CDDP group was slightly higher than that of the T@CDDP group, but it was much lower in kidneys. This indicated that our HT@CDDP NPs could reduce the renal toxicity of CDDP, which is one of the most significant limitations in clinical use. As shown in **Table S1**, we detected changes in blood urea nitrogen (BUN), creatinine (Cr), aspartate aminotransferase (AST), and alanine aminotransferase (ALT) at 2 and 4 weeks postinjection. To determine whether there was any substantial damage to livers and kidneys, we dissected the rats 6 weeks postinjection and conducted a histological analysis. As shown in **Figure S17D**, H&E staining indicated that there was no obvious damage to the livers and kidneys. Therefore, the HT@CDDP NPs have been shown to accumulate at tumor sites and reduce renal toxicity compared to T@CDDP. Through *in vivo* experiments, we confirmed that in short periods, the NPs did less damage to living organs than T@CDDP. Moreover, the NPs show a good bio-degradation property (**Figure S19**). The active and passive targeting characteristics of nanomaterials reduce the damage caused by CDDP to normal tissues. In addition, the low toxicity of TQTPA and biocompatibility of HA contribute to the biosafety of the HT@CDDP NPs. Therefore, we can look forward in the future to the clinical translation of these NPs.
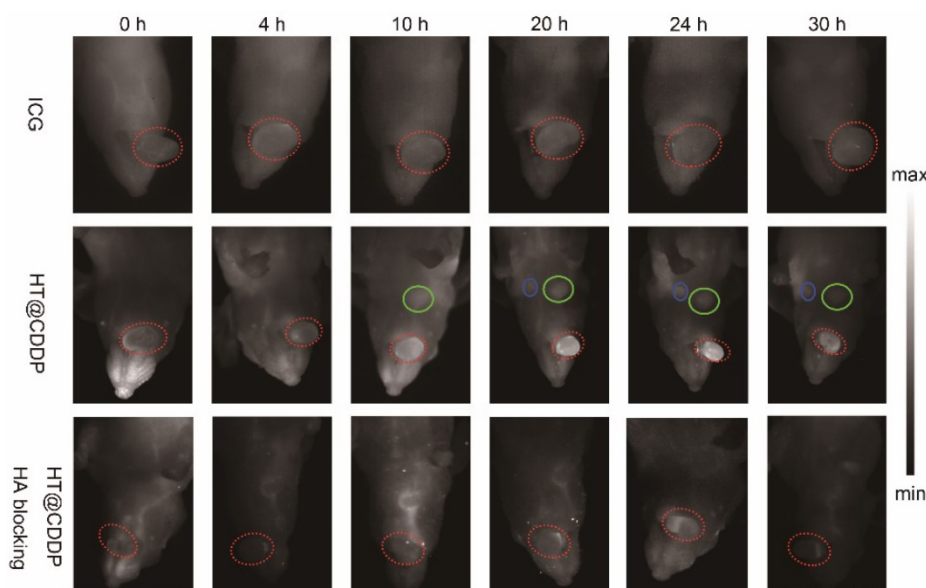

Figure 7. NIR-I/NIR-II images of HSC3 orthotopic tumor-bearing mice (n = 3 per group). The images were acquired immediately, 4 h, 10 h, 20 h, 24 h, and 30 h after tail vein injection of ICG and HT@CDDP NPs, with or without excess HA blocking. Red circles indicate tumors. Green and blue circles indicate two lymph nodes. (NIR-I: 808 nm excitation, 830 LP and 300 ms; NIR-II: 1064 LP and 2000 ms).
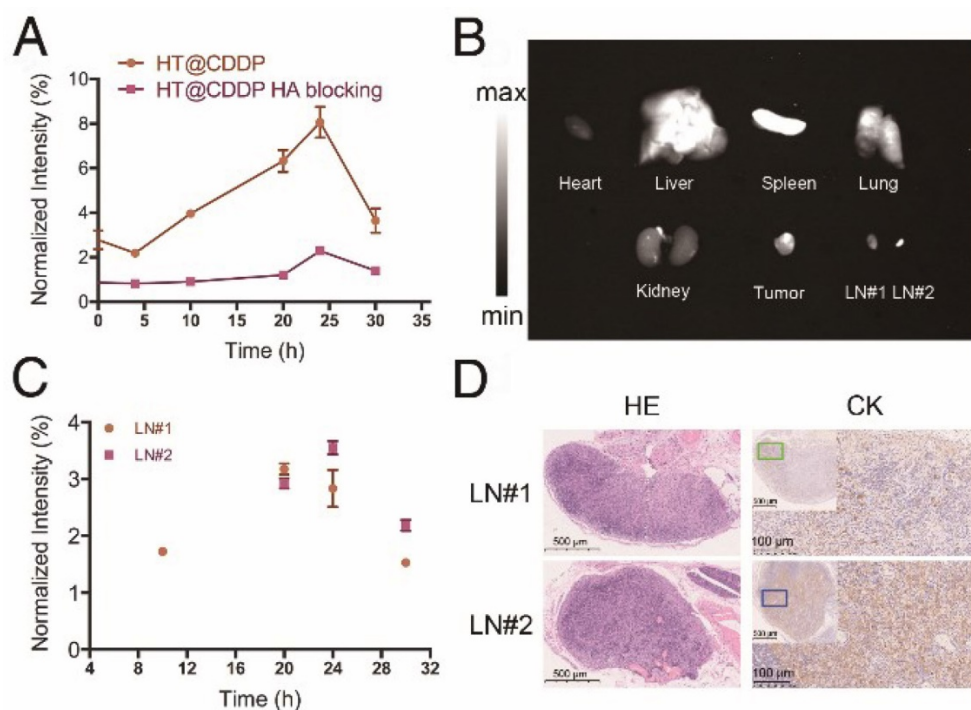
Figure 8. The fluorescence intensity of tumor, metastatic lymph nodes and dissected organs. (A) The NIR-II SBR (signal intensity-to- -background ratio) of tumors in the HT@CDDP and HA blocking groups at different time points. Data shown here are mean ± SE (n=3). **(B)** NIR-II imaging of dissected organs, tumor tissues, and lymph nodes at 30 h postinjection. **(C)** The NIR-II signal intensity of lymph nodes at different time points. The results represent mean ± SE (n=3). **(D)** HE and CK staining of LN#1 and LN#2.
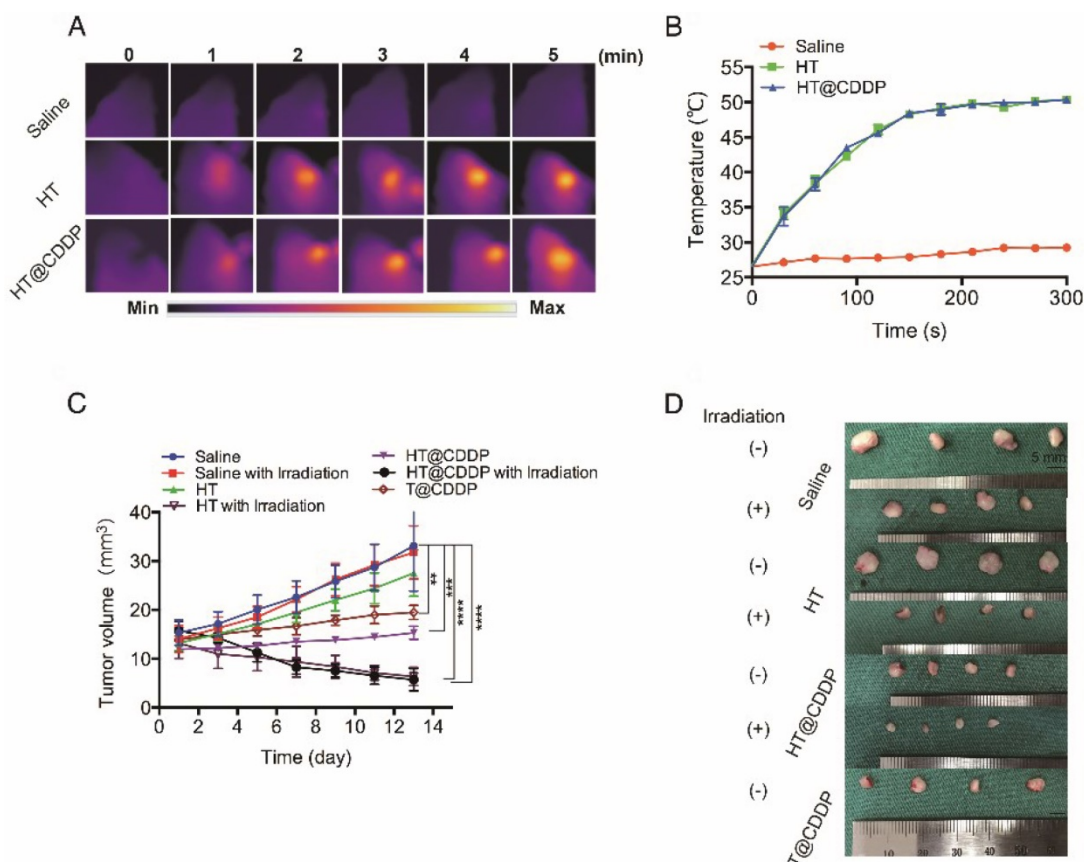

Figure 9. The photothermal property *in vivo* and anti-tumor ability of NPs. (A) Heat map of the tumors in vivo after injecting HT@CDDP and HT. The range min-max represents 24.2℃ -54.3 ℃. **(B)** The *in vivo* temperature curves. The results represent mean ± SE (n=4). **(C)** *In vivo* anti-tumor efficacy is detected by tumor volumes and the results are expressed as the mean ± SE (n = 4), *P < 0.05, **P < 0.01. **(D)** Mice tumor photographs.
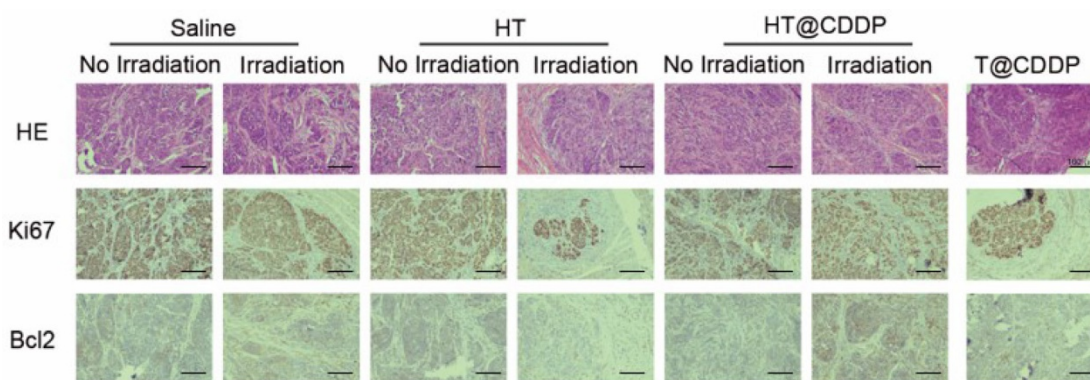
Figure 10. **HE and IHC staining of dissected tumors.** HE, Ki67, and Bcl2 staining of tumors for evaluating anti-tumor effect as well as the effect of inhibiting tumor proliferation and promoting cell apoptosis.

Conclusions

In this study, we synthesized a new NIR-II molecule, TQTPA, with stable photothermal characteristics, which are essential for NIR-II imaging and PTT. On the basis of a nano-technique, we synthesized HT@CDDP NPs with a good water solubility and dimensional stability. OSCC cell lines expressing high levels of CD44 receptors showed an obvious NIR-II signal after incubation with HT@CDDP, whereas the signal declined significantly when the cells were blocked with anti-CD44 antibody. HT@CDDP can be used for tumor delineation, metastatic lymph node detection, lymphatic system imaging and combined chemo-PTT.

Abbreviations

AAS: atomic absorption spectroscopy; CDDP: *cis*-dichlorodiammine platinum; CK: cytokeratin; DLS: dynamic light scattering; EPR: enhanced permeability and retention effect; HA: hyaluronic acid; H&E: hematoxylin &eosin staining; ICG: indocyanine green; NIR: near-infrared; NPs: nanoparticles; OSCC: oral squamous cell carcinoma; PTT: photothermal therapy; SBR: signal-to- background ratio; TEM: transmission electron microscope.

Acknowledgements

Supplementary Material

Supplementary figures and tables.
http://www.thno.org/v09p0391s1.pdf

Competing Interests

The authors have declared that no competing interest exists.

References

1. Siegel R, Naishadham D, Jemal A. Cancer statistics, 2012. CA: a cancer journal for clinicians. 2012; 62: 10-29.
2. Gupta S, Kong W, Peng Y, Miao Q, Mackillop WJ. Temporal trends in the incidence and survival of cancers of the upper aerodigestive tract in Ontario and the United States. International journal of cancer Journal international du cancer. 2009; 125: 2159-65.
3. Argiris A, Karamouzis MV, Raben D, Ferris RL. Head and neck cancer. Lancet. 2008; 371: 1695-709.
4. Hinni ML, Ferlito A, Brandwein-Gensler MS, Takes RP, Silver CE, Westra WH, et al. Surgical margins in head and neck cancer: a contemporary review. Head & neck. 2013; 35: 1362-70.
5. Pitman KT. Sentinel node localization in head and neck tumors. Semin Nucl Med. 2005; 35: 253-6.
6. Atallah I, Milet C, Henry M, Josserand V, Reyt E, Coll JL, et al. Near-infrared fluorescence imaging-guided surgery improves recurrence-free survival rate in novel orthotopic animal model of head and neck squamous cell carcinoma. Head & neck. 2016; 38 Suppl 1: E246-55.
7. Eldeeb H, Macmillan C, Elwell C, Hammod A. The effect of the surgical margins on the outcome of patients with head and neck squamous cell carcinoma: single institution experience. Cancer Biol Med. 2012; 9: 29-33.
8. Shou K, Qu C, Sun Y, Chen H, Chen S, Zhang L, et al. Multifunctional biomedical imaging in physiological and pathological conditions using a NIR-II probe. Adv Funct Mater. 2017; 27.
9. Jiang Y, Pu K. Molecular Fluorescence and Photoacoustic Imaging in the Second Near-Infrared Optical Window Using Organic Contrast Agents. Advanced Biosystems. 2018; 2: 1700262.
10. Xu G, Yan Q, Lv X, Zhu Y, Xin K, Shi B, et al. Imaging of Colorectal Cancers Using Activatable Nanoprobes with Second Near-Infrared Window Emission. Angewandte Chemie. 2018; 57: 3626-30.
11. Hong G, Antaris AL, Dai H. Near-infrared fluorophores for biomedical imaging. Nature Biomedical Engineering. 2017; 1: 0010.
12. Shi B, Yan Q, Tang J, Xin K, Zhang J, Zhu Y, et al. Hydrogen sulfide-activatable second near-infrared fluorescent nanoassemblies for targeted photothermal cancer therapy. Nano Lett. 2018; 18:6411-6416.
13. Lin SL, Chen ZR, Chang CA. Nd(3+) sensitized core-shell-shell nanocomposites loaded with IR806 dye for photothermal therapy and up-conversion luminescence imaging by a single wavelength NIR light irradiation. Nanotheranostics. 2018; 2: 243-57.
14. Xu F, Zhao Y, Hu M, Zhang P, Kong N, Liu R, et al. Lanthanide-doped core-shell nanoparticles as a multimodality platform for imaging and photodynamic therapy. Chemical communications. 2018; 54: 9525-8.
15. Zhen X, Zhang J, Huang J, Xie C, Miao Q, Pu K. Macrotheranostic Probe with Disease-Activated Near-Infrared Fluorescence, Photoacoustic, and Photothermal Signals for Imaging-Guided Therapy. Angewandte Chemie. 2018; 57: 7804-8.
16. Xu Y, Tian M, Zhang H, Xiao Y, Hong X, Sun Y. Recent development on peptide-based probes for multifunctional biomedical imaging. Chinese Chemical Letters. 2018; 29: 1093-7.

17. Tao W, Ji X, Xu X, Islam MA, Li Z, Chen S, et al. Antimonene Quantum Dots: Synthesis and Application as Near-Infrared Photothermal Agents for Effective Cancer Therapy. Angewandte Chemie. 2017; 56: 11896-900.

18. Tao W, Ji X, Zhu X, Li L, Wang J, Zhang Y, et al. Two-Dimensional Antimonene-Based Photonic Nanomedicine for Cancer Theranostics. Advanced materials. 2018; 30: e1802061.

19. Zhao P, Xu Q, Tao J, Jin Z, Pan Y, Yu C, et al. Near infrared quantum dots in biomedical applications: current status and future perspective. Wiley interdisciplinary reviews Nanomedicine and nanobiotechnology. 2018; 10: e1483.

20. Shen S, Zhang Y, Peng L, Du Y, Wang Q. Matchstick-shaped Ag2S-ZnS heteronanostructures preserving both UV/blue and near-infrared photoluminescence. Angewandte Chemie. 2011; 50: 7115-8.

21. Dong B, Li C, Chen G, Zhang Y, Zhang Y, Deng M, et al. Facile Synthesis of Highly Photoluminescent Ag2Se Quantum Dots as a New Fluorescent Probe in the Second Near-Infrared Window for in Vivo Imaging. Chemistry of Materials. 2013; 25: 2503-9.

22. Li C, Li F, Zhang Y, Zhang W, Zhang X, Wang Q. Real-time monitoring surface chemistry-dependent in vivo behaviors of protein nanocages via encapsulating an NIR-II Ag2S quantum dot. Acs Nano. 2015; 9: 12255-12263.

23. Du Y, Xu B, Fu T, Cai M, Li F, Zhang Y, et al. Near-infrared photoluminescent Ag2S quantum dots from a single source precursor. Journal of the American Chemical Society. 2010; 132: 1470-1471.

24. Qiu M, Wang D, Liang W, Liu L, Zhang Y, Chen X, et al. Novel concept of the smart NIR-light-controlled drug release of black phosphorus nanostructure for cancer therapy. Proc Natl Acad Sci U S A. 2018; 115: 501-6.

25. Qiu M, Ren WX, Jeong T, Won M, Park GY, Sang DK, et al. Omnipotent phosphorene: a next-generation, two-dimensional nanoplatform for multidisciplinary biomedical applications. Chemical Society reviews. 2018; 47: 5588-601.

26. Fan Q, Cheng K, Yang Z, Zhang R, Yang M, Hu X, et al. Perylene-diimide-based nanoparticles as highly efficient photoacoustic agents for deep brain tumor imaging in living mice. Adv Mater. 2015; 27: 843-7.

27. Wang H, Li X, Tse BW, Yang H, Thorling CA, Liu Y, et al. Indocyanine green-incorporating nanoparticles for cancer theranostics. Theranostics. 2018; 8: 1227-42.

28. Welsher K, Sherlock SP, Dai H. Deep-tissue anatomical imaging of mice using carbon nanotube fluorophores in the second near-infrared window. Proc Natl Acad Sci U S A. 2011; 108: 8943-8.

29. Chen G, Tian F, Li C, Zhang Y, Weng Z, Zhang Y, et al. In vivo real-time visualization of mesenchymal stem cells tropism for cutaneous regeneration using NIR-II fluorescence imaging. Biomaterials. 2015; 53: 265-73.

30. Antaris AL, Chen H, Cheng K, Sun Y, Hong G, Qu C, et al. A small-molecule dye for NIR-II imaging. Nature materials. 2016; 15: 235-42.

31. Antaris AL, Chen H, Diao S, Ma Z, Zhang Z, Zhu S, et al. A high quantum yield molecule-protein complex fluorophore for near-infrared II imaging. Nature communications. 2017; 8: 15269.

32. Feng Y, Zhu S, Antaris AL, Chen H, Xiao Y, Lu X, et al. Live imaging of follicle stimulating hormone receptors in gonads and bones using near infrared II fluorophore. Chemical science. 2017; 8: 3703-11.

33. Sun Y, Ding M, Zeng X, Xiao Y, Wu H, Zhou H, et al. Novel bright-emission small-molecule NIR-II fluorophores for in vivo tumor imaging and image-guided surgery. Chemical science. 2017; 8: 3489-93.

34. Sun Y, Qu C, Chen H, He M, Tang C, Shou K, et al. Novel benzo-bis(1,2,5-thiadiazole) fluorophores for in vivo NIR-II imaging of cancer. Chemical science. 2016; 7: 6203-7.

35. Xue Z, Zeng S, Hao J. Non-invasive through-skull brain vascular imaging and small tumor diagnosis based on NIR-II emissive lanthanide nanoprobes beyond 1500nm. Biomaterials. 2018; 171: 153-63.

36. Yang J, Hong X. New glowing dyes in vivo imaging with wavelengths beyond 1500 nm. Science China Chemistry. 2018; 61: 1869-1870.

37. Sun Y, Zeng X, Xiao Y, Liu C, Zhu H, Zhou H, et al. Novel dual-function near-infrared II fluorescence and PET probe for tumor delineation and image-guided surgery. Chem Sci. 2018; 9: 2092-7.

38. Kim S. Animal models of cancer in the head and neck region. Clin Exp Otorhinolaryngol. 2009; 2: 55-60.

39. Lu SL, Herrington H, Wang XJ. Mouse models for human head and neck squamous cell carcinomas. Head & neck. 2006; 28: 945-54.

40. Huang C, Yan T, Xu Z, Wang M, Zhou X, Jiang E,et al. Hypoxia enhances fusion of oral squamous carcinoma cells and epithelial cells partly via the epithelial-mesenchymal transition of epithelial cell. Biomed Research International. 2018, 5015203.

41. Joseph J, Harishankar M, Pillai A, Devi A. Hypoxia induced EMT: a review on the mechanism of tumor progression and metastasis in OSCC. Oral oncology. 2018; 80: 23-32.

42. Yoshiba S, Ito D, Nagumo T, Shirota T, Hatori M, Shintani S. Hypoxia induces resistance to 5-fluorouracil in oral cancer cells via G1 phase cell cycle arrest. Oral Oncol. 2009; 45: 109-115.

43. Huang CE, Yu CC, Hu FW, Chou MY, Tsai LL. Enhanced chemosensitivity by targeting Nanog in head and neck squamous cell carcinomas. Int J Mol Sci. 2014; 15: 14935-48.

44. Tonigold M, Rossmann A, Meinold M, Bette M, Marken M, Henkenius K, et al. A cisplatin-resistant head and neck cancer cell line with cytoplasmic p53(mut) exhibits ATP-binding cassette transporter upregulation and high glutathione levels. J Cancer Res Clin Oncol. 2014; 140: 1689-704.

45. Bai X, Ni J, Beretov J, Graham P, Li Y. Cancer stem cell in breast cancer therapeutic resistance. Cancer treatment reviews. 2018; 69: 152-63.

46. Zhou J, Wang X, Du L, Zhao L, Lei F, Ouyang W, et al. Effect of hyperthermia on the apoptosis and proliferation of CaSki cells. Mol Med Rep. 2011; 4: 187-91.

47. Wust P, Hildebrandt B, Sreenivasa G, Rau B, Gellermann J, Riess H, et al. Hyperthermia in combined treatment of cancer. Lancet Oncol. 2002; 3: 487-97.

48. Torchilin V. Tumor delivery of macromolecular drugs based on the EPR effect. Adv Drug Deliv Rev. 2011; 63: 131-5.

49. Maeda H. Toward a full understanding of the EPR effect in primary and metastatic tumors as well as issues related to its heterogeneity. Adv Drug Deliv Rev. 2015; 91: 3-6.

50. Maeda H, Nakamura H, Fang J. The EPR effect for macromolecular drug delivery to solid tumors: Improvement of tumor uptake, lowering of systemic toxicity, and distinct tumor imaging in vivo. Adv Drug Deliv Rev. 2013; 65: 71-9.

51. Huang Y, Yao X, Zhang R, Ouyang L, Jiang R, Liu X, et al. Cationic conjugated polymer/fluoresceinamine-hyaluronan complex for sensitive fluorescence detection of CD44 and tumor-targeted cell imaging. ACS Appl Mater Interfaces. 2014; 6: 19144-53.

52. Cai S, Alhowyan AA, Yang Q, Forrest WC, Shnayder Y, Forrest ML. Cellular uptake and internalization of hyaluronan-based doxorubicin and cisplatin conjugates. J Drug Target. 2014; 22: 648-57.

53. Chen J, Zhou J, Lu J, Xiong H, Shi X, Gong L. Significance of CD44 expression in head and neck cancer: a systemic review and meta-analysis. BMC Cancer. 2014; 14: 15.

54. Nam K, Oh S, Lee KM, Yoo SA, Shin I. CD44 regulates cell proliferation, migration, and invasion via modulation of c-Src transcription in human breast cancer cells. Cell Signal. 2015; 27: 1882-94.

55. Mochida Y, Cabral H, Miura Y, Albertini F, Fukushima S, Osada K, et al. Bundled assembly of helical nanostructures in polymeric micelles loaded with platinum drugs enhancing therapeutic efficiency against pancreatic tumor. ACS Nano. 2014; 8: 6724-38.

56. Fan X, Zhao X, Qu X, Fang J. pH sensitive polymeric complex of cisplatin with hyaluronic acid exhibits tumor-targeted delivery and improved in vivo antitumor effect. Int J Pharm. 2015; 496: 644-53.

57. Cai S, Xie Y, Davies NM, Cohen MS, Forrest ML. Pharmacokinetics and disposition of a localized lymphatic polymeric hyaluronan conjugate of cisplatin in rodents. J Pharm Sci. 2010; 99: 2664-71.

58. Jeong YI, Kim ST, Jin SG, Ryu HH, Jin YH, Jung TY, et al. Cisplatin-incorporated hyaluronic acid nanoparticles based on ion-complex formation. J Pharm Sci. 2008; 97: 1268-76.

59. Saisyo A, Nakamura H, Fang J, Tsukigawa K, Greish K, Furukawa H, et al. pH-sensitive polymeric cisplatin-ion complex with styrene-maleic acid copolymer exhibits tumor-selective drug delivery and antitumor activity as a result of the enhanced permeability and retention effect. Colloids Surf B Biointerfaces. 2016; 138: 128-37.

60. Seiichi O, Shota H, Yuki A, Shigenobu E, Hironori Y, Hironori S, et al. Intraperitoneal delivery of cisplatin via a hyaluronan-based Nanogel/in situ cross-linkable hydrogel hybrid system for peritoneal dissemination of gastric cancer. Mol. Phamaceutics. 2017; 14: 3105-3113.

61. Liu B, Han L, Liu J, Han S, Chen Z, Jiang L. Co-delivery of paclitaxel and TOS-cisplatin via TAT-targeted solid lipid nanoparticles with synergistic antitumor activity against cervical cancer. Int J Nanomedicine. 2017; 12:955-968.

62. McAtee CO, Barycki JJ, Simpson MA. Emerging roles for hyaluronidase in cancer metastasis and therapy. Adv Cancer Res. 2014; 123: 1-34.

63. Pavan M, Beninatto R, Galesso D, Panfilo S, Vaccaro S, Messina L, et al. A new potential spreading factor: Streptomyces koganeiensis hyaluronidase. A comparative study with bovine testes hyaluronidase and recombinant human hyaluronidase of the HA degradation in ECM. Biochim Biophys Acta. 2016; 1860: 661-8.

64. Zhou J, Jiang Y, Hou s, Upputuri P, Wu D, Li J, et al. Compact plasmonic blackbody for cancer theranosis in the near-infrared II window. Acs Nano.2018; 12(3): 2643-2651.
65. Lyu Y, Xie C, Chechetka S, Miyako E, Pu K. Semiconducting polymer nanobioconjugates for targeted photothermal activiation of neurons. J. Am. Chem. Soc. 2016; 138: 9049-9052.
66. Jung H, Verwilst P, Sharma A, Shin J, Sessler J, Kim J. Organic molecule-based photothermal agents: an expanding photothermal therapy universe. Chem Soc Rev. 2018; 47:2280-2297.